RESEARCH ARTICLE

Removal of cesium and strontium for radioactive wastewater by Prussian blue nanorods

Chuqing Yao[1] · Yaodong Dai[1] · Shuquan Chang[1] · Haiqian Zhang[1]

Abstract

In this work, novel Prussian blue tetragonal nanorods were prepared by template-free solvothermal methods to remove radionuclide Cs and Sr. The as-prepared Prussian blue nanorods were identified and characterized by scanning electron microscopy, transmission electron microscope, Fourier transform infrared spectroscopic, thermogravimetric analysis, zeta potential, and surface analysis, and its sorption performance was tested by batch experiments. Our results suggest that Prussian blue nanorods exhibited better adsorption performance than co-precipitation PB or Prussian blue analogue composites. Thermodynamic analysis implied that the adsorption process was spontaneous and endothermic which was described well with the Langmuir isotherm and pseudo-second-order equation. The maximum adsorption capacity of PB nanorod was estimated to be 194.26 mg g^{-1} and 256.62 mg g^{-1} for Cs$^+$ and Sr^{2+}(adsorbate concentration at 500 mg L^{-1}, the temperature at 298 k, pH at 7.0). Moreover, the experimental results showed that the Prussian blue nanorods have high crystallinity, few crystal defects, and good stability under alkaline conditions. The adsorption mechanism of Cs$^+$ and Sr^{2+} was studied by X-ray photoelectron spectroscopy, X-ray diffraction, and ^{57}Fe Mössbauer spectroscopy. The results revealed that Cs$^+$ entered the PB crystal to generate a new phase, and most of Sr^{2+} was trapped in the internal crystal and the other exchanged Fe^{2+}. Furthermore, the effect of co-existing ions and pH on PB adsorption process was also investigated. The results suggest that PB nanorods were an outstanding candidate for removing Cs$^+$ and Sr^{2+} from radioactive wastewater.

Keywords Radioactive wastewater treatment · Prussian blue · Adsorption · Cesium · Strontium

Introduction

With the rapid development of nuclear energy applications in recent years, nuclear and radiation safety has aroused public attention. Decontaminating the large amount of radioactive wastewater generated in nuclear energy applications has become an urgent problem to be solved. Radioactive strontium and cesium are the primary contaminants in low-level radioactive wastewater because of their serious hazard to the natural environment and human health. How to remove these radionuclides efficiently from polluted water was the focus of the research. Prussian blue

$(Fe_4[Fe(CN)_6]_3·xH_2O)$ was a kind of common adsorbent that attracted much attention because of its excellent adsorption capacity, good selectivity, and low price (Wu et al. 2005). The classic synthesis method of Prussian blue was potassium ferrocyanide and ferric chloride co-precipitated in an aqueous solution. The obtained Prussian blue was agglomerated nanoparticle co-polymer which significantly reduced the number of adsorption sites. In recent, Prussian blue with a particular shape has been prepared by diverse synthesis methods, such as Vaucher et al. (2000) synthesized superlattice Prussian blue nanocubes in reverse microemulsion; the length range of nanocube was 10 to 30 nm. Hu et al. (2011) prepared Prussian blue analogue porous nanocube in the presence of PVP, and PBA nanocube presents a huge BET surface and excellent adsorption efficiency of Pb^{2+}(94% in 10 mg L^{-1}). Bu et al. (2015) used self-aggregation and orient attachment of Prussian blue particle synthesized three-dimensional hierarchical Prussian blue, and the 3D Prussian blue showed a high adsorption capacity of Cs$^+$ which was higher than commercial

✉ Yaodong Dai
yd_dai@sina.com

1 College of Material Science and Technology, Nanjing University of Aeronautics and Astronautics, Nanjing 211106, China

Prussian blue 95%. Ming Hu (Hu et al. 2012a, b; Hu et al. 2013) and Cai et al. (2016) used a unique method to synthesize Prussian blue cubes with hollow structures; the yolk-shell and yolk-double-shell PBA was obtained by hot hydrochloric acid etching in former research, and the other one prepared $Ni_3[Fe(CN)_6]_2$ box and cube-in-box by sacrificial template method which was based on the different solubility of PBA in alkaline solution.

Compared with other structures of Prussian blue, the one-dimensional (1D) structure was usually ignored in research. 1D nanomaterials have received much attention due to their unique morphology and great potential applications (Tiwari et al. 2012). 1D inorganic nanomaterials showed excellent adsorption capacity because they had more significant surface area and adsorption sites. Among the variety morphology of Prussia blue, one-dimensional structured PB was difficult to synthesize owing to its complex elemental constituent and crystal structure. The research on 1D Prussian blue was rare, and the main synthesis route was sacrificial template method. Zhou et al. (2002) fabricated Prussian blue nanotubes and nanowires by electrodeposition on porous anodic aluminum oxide. The size of Prussian blue depends on the pore diameter of anodic aluminum oxide template, and the obtained PB nanowires have diameters of 50 nm and lengths up to 4 μm. Yin et al. (2018) synthesized $Co_3[Fe(CN)_6]_2$ hollow structure with the prism, polyhedron, and sphere morphology by using cobalt acetate hydroxide, ZIF-67, and Co-glycerate precursor as a template, respectively. It was noticeable that the above methods were difficult to be applied in large-scale wastewater decontamination due to their high cost and low output. On the contrary, hydrothermal synthesis was easier to operate and cost less than the commonly nanomaterial synthesis method; the final products had uniform morphology and high purity. Hydrothermal reaction utilizes water under elevated pressures and temperatures above its critical point to increase the solubility of a solid and to speed up dissolution and recrystallization of precursor. Reverse microemulsion (water in oil) system was widely applied in synthesizing nanomaterials (Xu et al. 2005); microemulsion contained an aqueous phase which dispersed in oil phase and packaged by surfactant; aqueous phase provided an excellent reaction place for forming a specific shape. Microemulsion hydrothermal could effectively control the product's morphology by adjusting the water, oil, and surfactant ratio.

In this work, we successfully synthesized the tetragonal Prussian blue nanorod by microemulsion solvothermal method. The morphology, structure, and influence factor in growth process of PB nanorod were investigated. The obtained PB nanorods were utilized for the removal of strontium and cesium in simulated radioactive wastewater; the adsorption performance was tested at different contact times, adsorbate concentration, temperature, pH, and co-existing cations.

Experiment and characterization

Preparation of materials

All chemicals were purchased from Aladdin and without further purification. Prussian blue nanorods were synthesized by hydrothermal microemulsion method. In a typical experiment procedure, 0.405 mmol potassium ferricyanide and 0.405 mmol glucose were dissolved in 4.05 mL deionized water, 15 mmol cetyltrimethylammonium bromide (CTAB) and 65 mmol n-pentanol were added into 70 ml n-hexane, and then the two solutions were mixed and keep stirred until the microemulsion was optically transparent; after that, the microemulsion was transferred to 100-mL stainless Teflon-lined autoclave and maintained at 120℃ for 12 h; the stainless Teflon-lined autoclave was cooled at room temperature. Finally, the precipitate was separated by centrifugation and washed with chloroform and ethanol mixture solution several times. The final products were dried in a vacuum oven at 70℃ for 12 h. In order to investigate the influence of surfactant on Prussian blue morphology and micelle size, we synthesized Prussian blue in 7.5, 10, 17.5, and 20 mmol CTAB and other conditions not changed.

Materials characterization

Fourier transform infrared spectroscopic (FTIR) spectra were recorded on the Nicolet NEXUS870 FTIR spectrometer, using the transition mode and the wavelength range set from 4000 to 500 cm^{-1}. The morphology images of Prussian blue nanorod were acquired with FEI Quanta 650 scanning electron microscopy (SEM). The crystal structure and select area electron diffraction (SAED) of Prussian blue nanorod were obtained by FEI Tecnai G20 high-resolution transmission electron microscopy (HRTEM). Thermogravimetric analysis (TG) used TGA5500 from 30 to 800℃ in air. 77 K N_2 adsorption–desorption isotherms was measured by Micromeritics ASAP2460. Powder X-ray diffraction (XRD) patterns were measured by the Rigaku Ultima IV diffractometer using Cu Kα radiation from 5 to 90°. The zeta potentials of Prussian blue nanorods were measured by the Malvern Zetasizer Nano system (ZS 90, UK) with irradiation from a 633-nm He–Ne laser at various pHs from 2 to 11. The X-ray photoelectron spectroscopy (XPS) of Prussian nanorods before and after adsorption was measured on a Thermo ESCALAB 250XI instrument. The high-resolution spectra were collected and calibrated to the binding energy of C 1 s at 284.8 eV. Mössbauer spectrum was recorded using a WSSL-10 spectrometer at 300 K, and the γ-ray radioactive source was $^{57}Co/Rh$.

Adsorption procedure

The Prussian blue nanorod was tested for the adsorption of radioactive ^{90}Sr and ^{137}Cs from aqueous solutions at room

temperature using the batch technique. The radioactive wastewater containing ^{90}Sr and ^{137}Cs was simulated by Sr(NO$_3$)$_2$ and CsCl aqueous solution. Ten milligrams of sample was added in test tubes which contained 10 mL CsCl or Sr(NO$_3$)$_2$ solution, and the concentration was 500 mg L^{-1}, and the initial pH of solution was 7.0. Then the tubes were shaken on a vortex shaker for 6 h at 298 K. The effect of several variables of solution pH, contact time, solution temperature, and adsorbate concentration was also studied. The pH value of solution was adjusted from 2 to 11 by adding 0.01 M HCl and 0.01 M NaOH. The contact time was conducted from 0 to 6 h. The solution temperature was conducted at 298 k, 303 K, and 308 K. The adsorbate concentration was conducted at 100, 200, and 500 mg L^{-1}. At the end of adsorption experiments, the concentration of strontium that remained in solution was measured by atomic absorption spectrophotometer (AAS, TAS-990). In order to investigate the effect of co-existing ions for adsorption process, the tested solution contained 0.01, 0.1, and 1 mol L^{-1} NaCl, KCl, MgCl$_2$, and CaCl$_2$, respectively. The initial concentration of Cs$^+$ and Sr^{2+} in this solution was adjusted to 50 mg L^{-1}. The artificial seawater composition was from a previous article, and the concentration of Cs$^+$ and Sr^{2+} was 50 mg L^{-1} in this solution (Falyouna et al. 2020).

The uptake amounts per gram of Prussian blue nanorods were evaluated from the change in solution concentration using Eq. (1):

$$q = \frac{C_0 - C_t}{M} \times V \tag{1}$$

The distribution coefficient was calculated by Eq. (2):

$$K_d = \frac{C_0 - C_t}{C_t} \times \frac{V}{M} \tag{2}$$

where q (mg g^{-1}) is the uptake capacity, C_0 (mgL^{-1}) is the initial concentration of strontium solution, C_t (mg L^{-1}) is the final concentration in aqueous solution, M (g) is the mass of adsorbent, V (L) is the volume of the solution, and K_d (mL g^{-1}) is the distribution coefficient.

Result and discussion

Characterization of Prussian blue nanorod

The morphology of Prussian blue nanorod was shown in Fig. 1a and b. It was observed that many tetragonal nanorods were stacked together, and the aspect ratio of PB nanorods was greater than 10. The length range of nanorods was from 1.5 to 3 μm, and the diameter of nanorod was nearly 150 nm. Figure 1c is the HRTEM image of Prussian blue nanorod, in which PB nanorod had a regular rectangle lengthwise section and a dense crystal

surface, and the size of PB nanorod in HRTEM image was similar to Fig. 1a. XRD and HRTEM characterized the crystal structure of Prussian blue nanorod. The XRD pattern of PB nanorod was shown in Fig. 2a. All reflection peaks were indexed to the ferric ferrocyanide (JCPDS 73–0687) with the lattice constants of $a = 10.13$ Å. The extremely narrow and intensity peak indicated that the as-obtained products may had greater crystalline and unique morphology. Figure 1d is the HRTEM image of PB nanorod; the measured lattice fringe with an interplanar spacing of about 0.506 nm was indexed to the (200) plane of PB nanorod (Kim et al. 2017), which indicated that Prussian blue nuclei grown as nanorod in the direction of [100], this result also agreed well with XRD pattern. Figure 1e shows the SAED image of PB nanorod, which indicated that PB nanorod was a single crystal and faced-centered cubic structure.

FT-IR spectrum was used qualitatively to analyze the chemical group of the samples. Figure 2b shows the FT-IR spectrum of Prussian blue nanorod. The adsorption peak at 3424 cm^{-1} was due to nonsymmetric stretching vibration of -OH, ascribed to crystal H$_2$O in Prussian blue. The sharp peaks at 2070 and 595 cm^{-1} were ascribed to the vibration of C≡N and Fe-CN bond (Feng et al. 2019), confirming that the final products were Prussian blue. The peak at 2911, 2834, and 1410 cm^{-1} revealed the symmetric and asymmetric stretching vibration of CH$_2$ and the vibration of C-H bend, which are all from the residual CTAB on the PB surface (Andrew Lin et al. 2015).

TG curves calculated the water content of PB nanorod from room temperature to 250℃ (Liu et al. 2015); the PB nanorod only lost 8.9wt% of the total weight, indicating that PB nanorod possessed few zeolitic water and Fe(CN)$_6$ vacancies, which gave them more vacancies to accommodate other ions.

The N$_2$ adsorption–desorption isotherms and pore size distribution of PB nanorods were shown in Fig. 3b; the calculated Brunauer–Emmett–Teller (BET) surface area was 4.4392 m^2 g^{-1}, and the total pore volume was 0.0126 cm^3 g^{-1}.

The zeta potential for PB nanorods was displayed in Fig. 3c at various pH values. The result showed that PB nanorods are negatively charged at pH ranging from 2 to 10, with the isoelectric point of PB at a pH value between 2 and 3. Especially, the zeta potential of PB was as low as -38.53 mv; thus, the results were attributed to the modification by the carboxy group which increased the negative surface charge and the electrostatic repulsion between the adsorbent powders, which could be beneficial for the electrostatic attraction of positive ions.

In order to investigate the morphology of PB nanorods under different growth conditions, we carried out a series of controlled experiments. CTAB was a commonly cationic

Fig. 1 SEM (**a** and **b**), HRTEM (**c** and **d**) and SAED pattern (**e**) images of PB nanorod
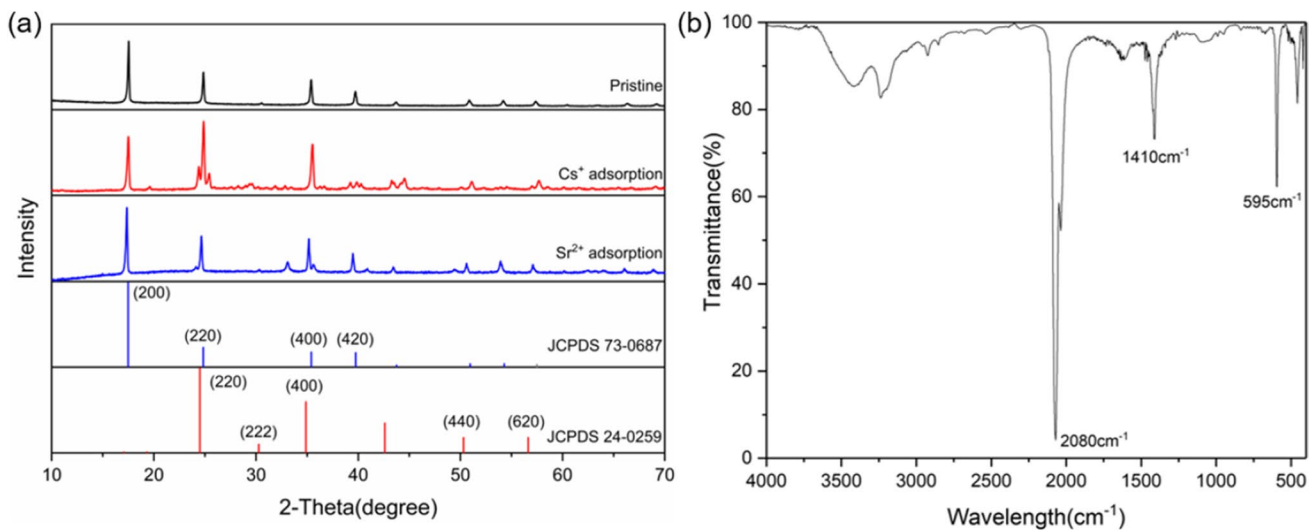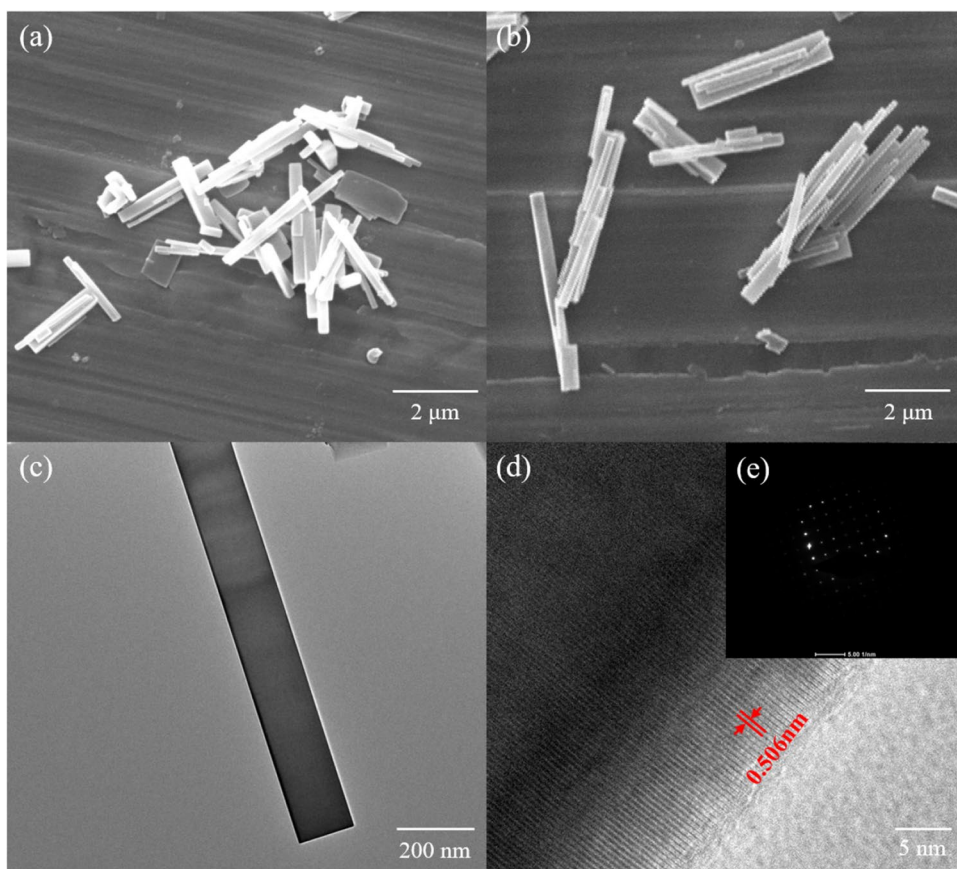

Fig. 2 XRD pattern (**a**) and FT-IR spectrum (**b**) of Prussian blue nanorod

surfactant that played a dominant role in microemulsion formation. Figure 4 presents the reaction products of 5 mmol, 7.5 mmol, 17.5 mmol, and 20 mmol CTAB, respectively. In Fig. 4a and b, the reaction products at low concentration of CTAB contained a lot of lamellar PB, the products at 7.5 mmol CTAB had a larger proportion of rod-like Prussian blue, and the lamellar PB was more regular than the products of 5 mmol. With the concentration of CTAB increased, the amount of lamellar PB decreased, and the proportion of one dimensional structured PB in as-obtained products
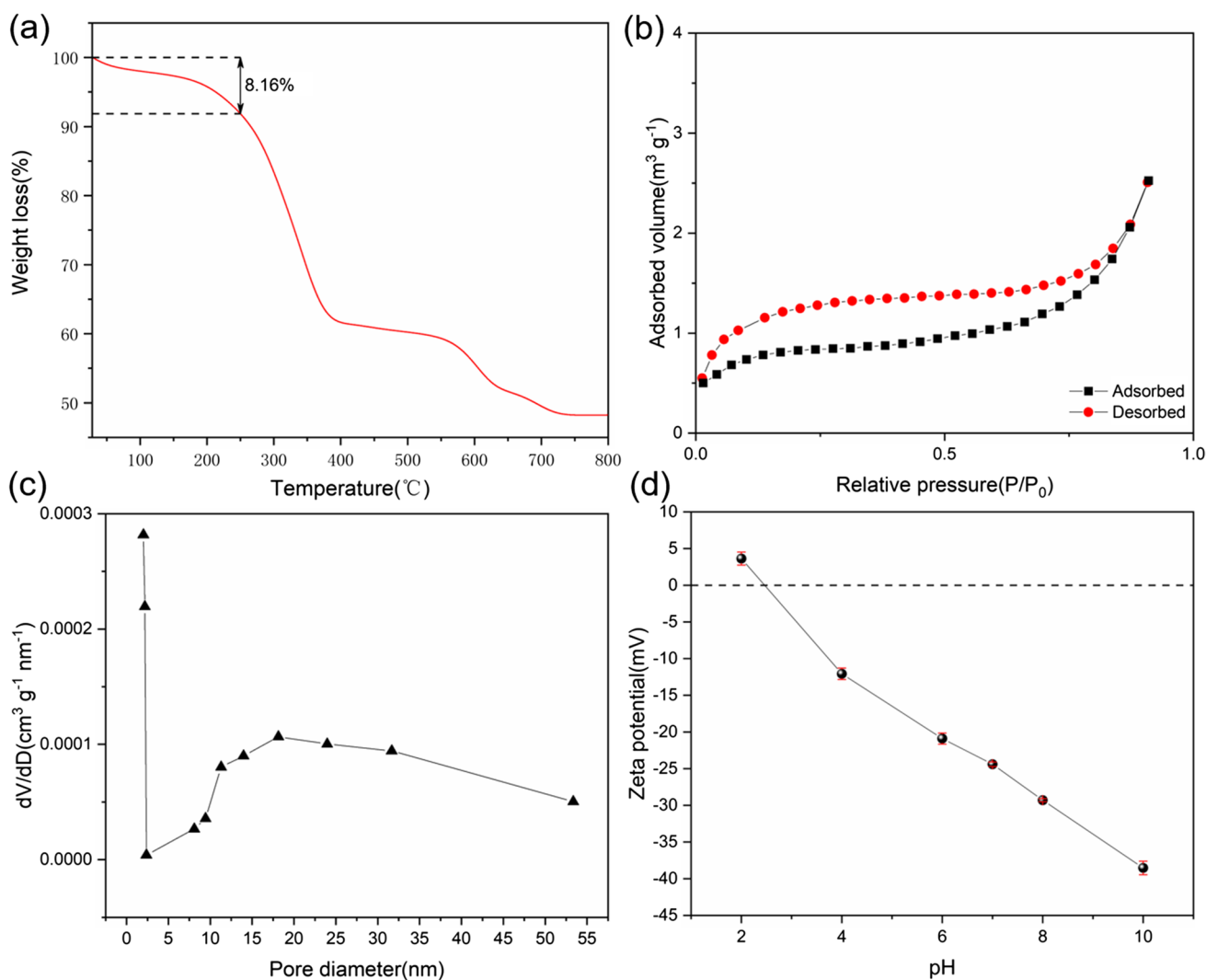
Fig. 3 **a** TG curve, **b** N_2 adsorption–desorption isotherms, **c** pore size distribution of PB nanorods and **d** zeta potential for PB nanorods at various pH

was increased. In Fig. 4c, the tetragonal PB rod width was close to 1 μm, and several PB nanorods were agglomerated, forming a sheet of Prussian blue. When the CTAB amount increased to 20 mmol, the final products contained many unregular Prussian blue cuboids with a width ranging from 300 nm to 2 μm and a length ranging from 1.5 to 3 μm. According to the above SEM images, the content of CTAB in solvent greatly influenced the final products morphology. Some research showed that bromine ions released by CTAB were preferential chemisorption on [100] facet of crystal (Xiong et al. 2007; Xiong and Xia 2007). At a low concentration of Br, some crystal facets not coated by bromine ions induced Prussian blue seed to grow in both directions, thus forming two-dimensional lamellar PB. As the concentration of Br ions increased, the lamellar products gradually decreased until they disappeared. However, the aggregate PB nanorods were increasing, and the large PB bars appeared frequently. According to the experiment result, it was obvious that the final products which reacted in 15 mmol CTAB conditions were suitable radioactive nuclide adsorbents.

Adsorption kinetics

Figure 5 displays the adsorption capacity of Prussian blue nanorod for Cs^+ and Sr^{2+} at different time intervals in various initial concentrations. It was observed that the adsorption capacity increased with time extension for all concentrations at initial stage, and then adsorption rate was slowed down and reached adsorption equilibrium 2 h later. On changing the initial ions concentration as 100, 200, and 500 mg L^{-1}, the equilibrium adsorption amount was 90.65, 157.05, and 206.92 mg g^{-1} for Cs^+ and 99.90, 189.92, and 270.75 mg g^{-1} for Sr^{2+}, which is due to the driving force of the concentration gradient overcame mass transfer resistance of ions between the aqueous and solid phase (Demirbas et al. 2009).

Fig. 4 SEM images of PB obtained from different amount of CTAB. **a** 5 mmol, **b** 7.5 mmol, **c** 17.5 mmol, **d** 20 mmol
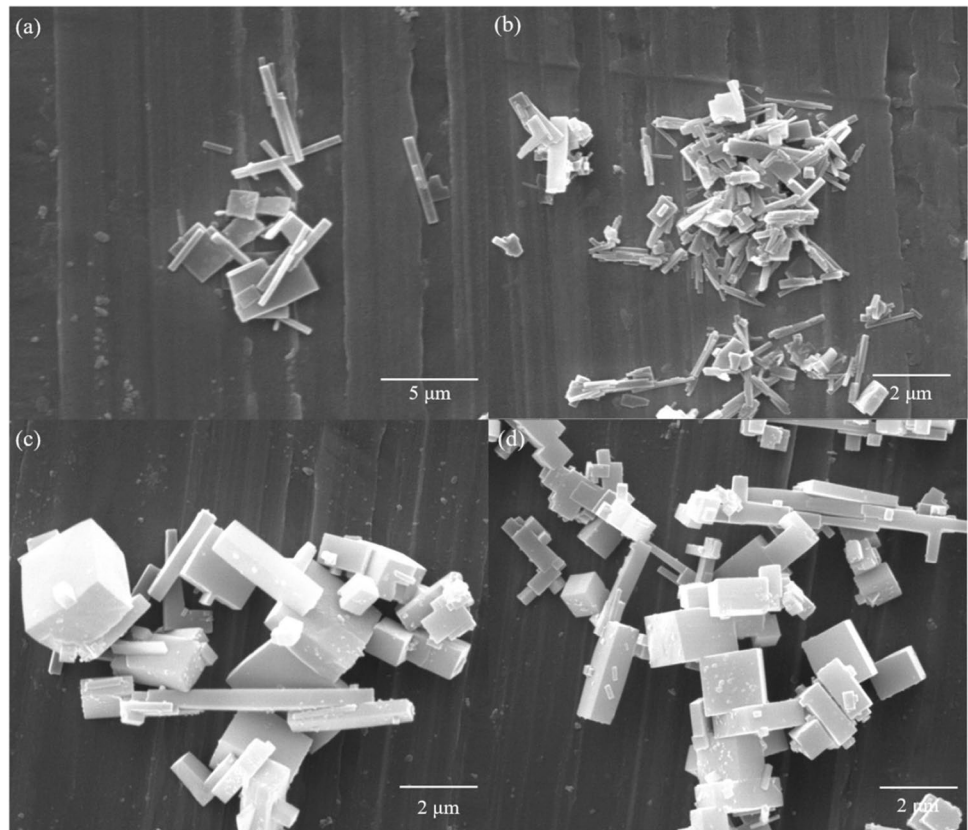
To further investigate the adsorption process on PB nanorods, the adsorption kinetics data were calculated according to the pseudo-first-order equation, pseudo-second-order equation, and Elovich equation (Ahrouch et al. 2019; Gupta et al. 2019). These equations were shown in Eqs. (3)–(5).

$$q_t = q_e(1 - e^{-k_1 t}) \tag{3}$$

$$q_t = \frac{q_e^2 k_2 t}{1 + q_e k_2 t} \tag{4}$$

$$q_t = b\ln(ab) + b\ln(t) \tag{5}$$

where q_e and q_t were the adsorption amount (mg g^{-1}) at the equilibrium and at time t (min), respectively. k_1(min^{-1}) and k_2 (g (mg g)$^{-1}$) were the rate constants of pseudo-first-order and pseudo-second-order equation. In Elovich equation, a represents initial adsorb rate (mg (g min)$^{-1}$), and b was desorption constant (g mg). The value of above parameters was listed in Table 1.

As shown in Table 1, the experimental data at different initial concentrations displayed excellent correspondence with the pseudo-second-order kinetic model. Its correlation coefficient was higher than pseudo-first-order and Elovich kinetic model. It confirmed that pseudo-second-order equation was

the best model to describe the adsorption process of PB nanorod. And the accordance with the pseudo-second-order reaction mechanism implied that the chemical processes controlled the adsorption processes, through sharing of electrons between adsorbent and adsorbate, or covalent forces, through the exchange of electrons between the particles involved (F. Zhang et al. 2015). k_2 was a constant related to the adsorbed rate; a large k_2 value represented an adsorption process that would take a short time to reach equilibrium (Ji et al. 2022). Therefore, the obtained large k_2 indicated that the PB nanorod took less time to remove Cs$^+$ and Sr^{2+}.

Adsorption isotherms and thermodynamics

The adsorption isotherm was an important pathway for understanding the character of adsorption system, and isotherm would provide physical chemistry data of the adsorption process. In order to fully understand the adsorption characteristic of cesium and strontium onto Prussian blue nanorod, the adsorption experiments data were fitted by three different isotherms.

The Langmuir isotherm assumed that adsorption occurs on a homogeneous surface, which means the enthalpy change and adsorption activation energy of each molecule are fixed, and the whole adsorption process is monolayer adsorption (Andrew Lin et al. 2015; Jin et al. 2012), as presented by
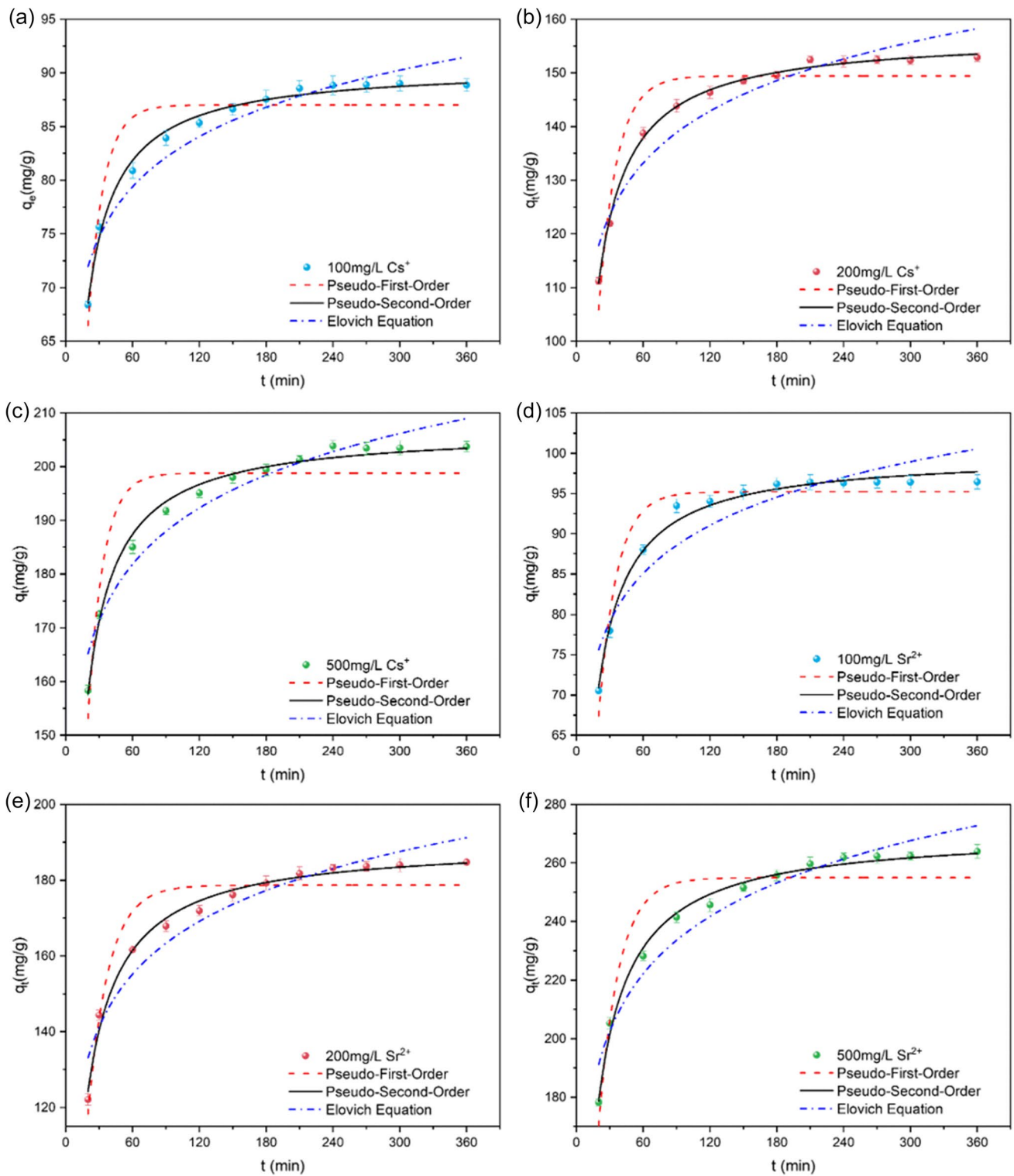
Fig. 5 Adsorption kinetic of PB nanorod at **a** 100, **b** 200, and **c** 500 mg L^{-1} Cs$^+$ solution and **d** 100, **e** 200, and **f** 500 mg L^{-1} Sr^{2+} solution

$$q_e = \frac{q_m k_L C_e}{1 + k_L C_e} \quad (6)$$

In addition, the separation factor R_L was the dimension constant obtained by Langmuir isotherm constant. The calculated equation was given by

$$R_L = \frac{1}{1 + k_L c_i} \quad (7)$$

The Freundlich isotherm assumed that adsorption occurs on heterogeneous surfaces and that adsorbents and adsorbents interacted with each other. Freundlich isotherm was often

Table 1 The fitting kinetic parameters of PB nanorod

C_0 (mg L^{-1})		Pseudo-first-order			Pseudo-second-order			Elovich equation		
		k_1 (min^{-1})	q_e (mg g^{-1})	r^2	k_2 (g (mg g)$^{-1}$)	q_e (mg g^{-1})	r^2	a	b	r^2
Cs$^+$	100	7.21×10^{-2}	87.02	0.87	1.71×10^{-3}	90.65	0.99	16.29	6.75	0.93
	200	6.16×10^{-2}	149.43	0.91	7.63×10^{-4}	157.05	0.99	16.42	13.97	0.92
	500	7.36×10^{-2}	198.81	0.85	7.73×10^{-4}	206.92	0.99	18.18	15.14	0.94
Sr^{2+}	100	6.15×10^{-2}	95.22	0.93	1.22×10^{-3}	99.90	0.99	7.21	8.62	0.87
	200	5.52×10^{-2}	178.65	0.90	4.97×10^{-4}	189.92	0.99	1.86	20.10	0.93
	500	5.51×10^{-2}	254.96	0.89	3.58×10^{-4}	270.75	0.99	1.53	28.25	0.95

applied in multilayer adsorption process (Cheng et al. 2019), as presented by

$$q_e = k_F c_e^{\frac{1}{n}} \tag{8}$$

The Redlich-Peterson isotherm was combination of the Langmuir and Freundlich isotherm, and the equation was given by

$$q_e = \frac{k_R c_e}{1 + a c_e^{\beta}} \tag{9}$$

where q_e and q_m were the adsorption amount (mg g^{-1}) at the equilibrium and maximum adsorption capacity. c_e (mg L^{-1}) and c_i were the concentration of strontium at the equilibrium and at the initial. k_L (L mg^{-1}), k_F (mg/g), k_R (L g^{-1}), and a (L mg^{-1}) were the Langmuir isotherm constant, Freundlich isotherm constant, and Redlich-Peterson isotherm constant, respectively. n and β were exponents. The value of parameters was summarized in Table 2.

Figure 6 shows the three isotherm models applied to experimental data. The adsorption amount of PB nanorod was increased with the temperature increasing both Cs$^+$ and Sr^{2+}. Langmuir isotherm exhibited the highest correlation coefficients among the three isotherms, which suggested that PB nanorod surface was homogenous and the adsorption process of Cs$^+$ and Sr^{2+} was monolayer adsorption. The maximum adsorption capacity calculated by Langmuir isotherm were 194.26, 232.58, and 284.74 mg g^{-1} for Cs$^+$ and 256.62, 290.94, and 316.58 mg g^{-1} for Sr^{2+} at 298 K, 303 K, and 308 K, respectively. The value of R_L would classify the shape of the isotherm as unfavorable ($R_L > 1$), linear ($R_L = 1$), irreversible ($R_L = 0$), and

favorable ($0 < R_L < 1$). We obtained a value of R_L of 0.29, 0.35, and 0.47 in Cs$^+$ sorption and 0.27, 0.35, and 0.38 in Sr^{2+} sorption; the value confirmed that the adsorption process of Cs$^+$ and Sr^{2+} onto PB nanorod was favorable. The R-P equation was approximate to Henry's law in low adsorbate concentration and the Freundlich isotherm in high concentration (Minitha et al. 2018). When exponent $\beta = 1$, the equation changed into the Langmuir model; when β trended to 0, the R-P equation was more Freundlich. The β values were all close to 1 in Table 2, which confirmed a Langmuir type mechanism.

Table 3 presents the reported various adsorbent for Cs$^+$ and Sr^{2+} adsorption along with their maximum adsorption capacity. The as-synthesized Prussian blue nanorod exhibited higher adsorption capacity than most reported adsorbents, especially for the removal of Sr^{2+}.

Adsorption thermodynamic was conducive to understanding the degree and driving force of the adsorption process and could deeply analyze the influence of various factors on the adsorption process. The thermodynamic parameters $\Delta G°$, $\Delta H°$, and $\Delta S°$ were calculated by Eqs. (10), (11), and (12) (Yu Liu 2009).

$$\Delta G° = \Delta H° - T\Delta S° \tag{10}$$

$$\Delta G° = RT \cdot \ln K° \tag{11}$$

$$\ln K = \frac{\Delta S°}{R} - \frac{\Delta H°}{RT} \tag{12}$$

$$K° = 1000 K_L M_A \tag{13}$$

Table 2 The fitting isotherm parameters of PB nanorod

T/K		Langmuir isotherm			Freundlich isotherm			Redlich-Peterson isotherm			
		k_L (L mg^{-1})	q_m (mg g^{-1})	r^2	k_F (mg/g)	n	r^2	β	k_R (L g^{-1})	a (L mg^{-1})	r^2
Cs$^+$	298 K	4.82×10^{-2}	194.26	0.99	60.51	5.08	0.96	0.94	12.29	8.94×10^{-2}	0.98
	303 K	3.61×10^{-2}	232.58	0.99	65.41	4.74	0.97	0.95	10.44	6.12×10^{-2}	0.99
	308 K	2.22×10^{-2}	284.74	0.99	51.18	3.56	0.95	1.05	5.61	1.42×10^{-2}	0.99
Sr^{2+}	298 K	5.20×10^{-2}	256.62	0.98	79.44	4.90	0.96	0.91	20.95	1.35×10^{-1}	0.98
	303 K	3.71×10^{-2}	290.94	0.99	74.49	4.31	0.92	1.02	10.16	3.11×10^{-2}	0.99
	308 K	3.23×10^{-2}	316.58	0.99	64.88	3.71	0.95	0.92	13.03	6.36×10^{-2}	0.99
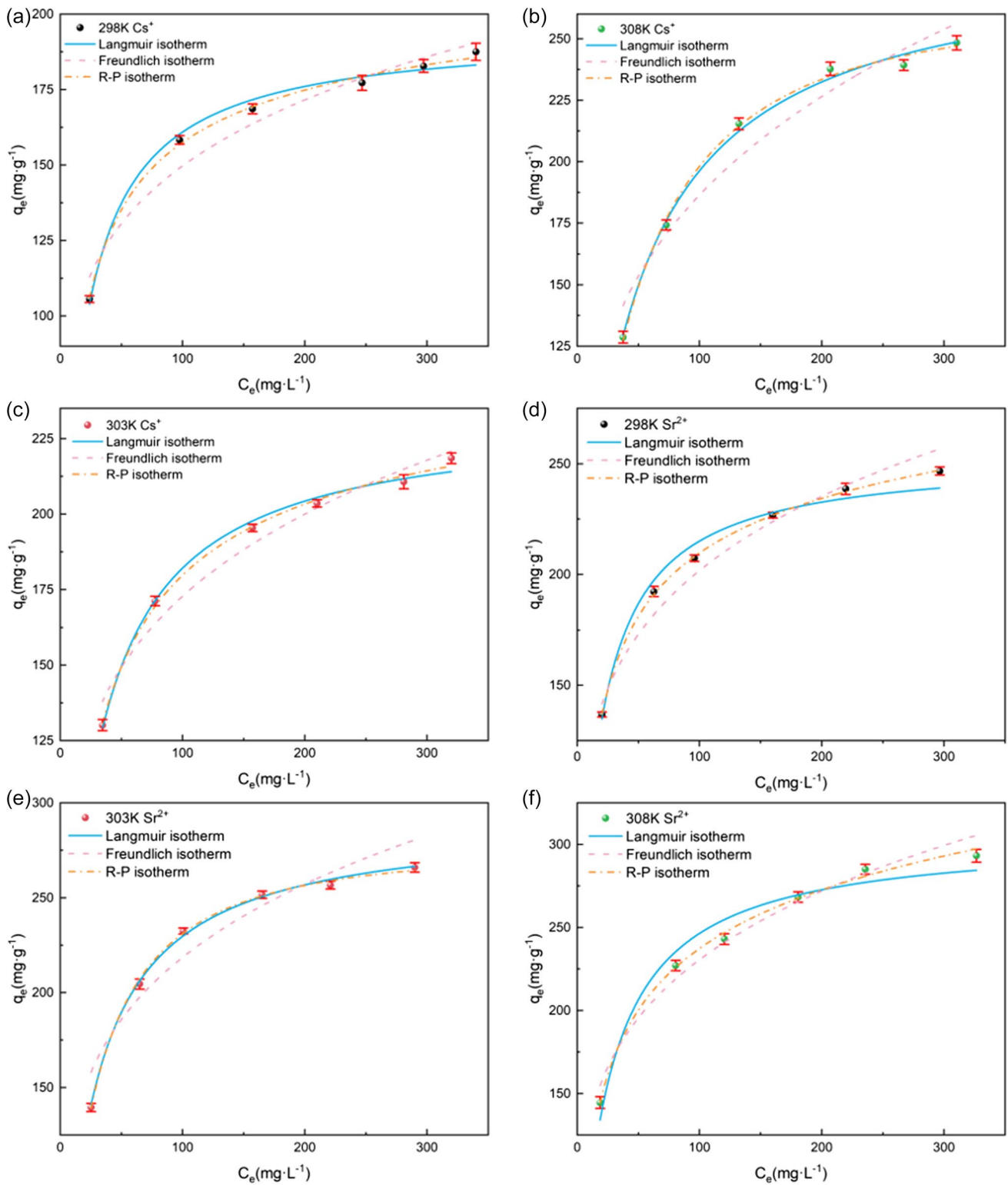
Fig. 6 Adsorption isotherms of PB nanorod for Cs$^+$ at 298 K (**a**), 303 K (**b**), 308 K (**c**), and Sr.$^{2+}$ at 298 K (**d**), 303 K (**e**), and 308 K (**f**)

where $\Delta G°$ was the standard Gibbs free energy, kJ mol^{-1}. $\Delta H°$ was the standard enthalpy, kJ/mol. $\Delta S°$ was the standard entropy, J (mol K)$^{-1}$. In some reference, the value of $K°$ could be approximately by

the Langmuir isotherm constant K_L, the value conversion between them is referred to Eq. (13) due to different units used in K° calculation, and M_A was adsorbate relative atomic mass (Liu 2009).

Table 3 Summary of reported adsorbent for Cs^+ and Sr^{2+} adsorption

Adsorbent	Q_{max}-Cs (mg g^{-1})	Q_{max}-Sr (mg g^{-1})	References
PB/Fe3O4/GO	55.6		Yang et al. (2014)
PB/RGOF	18.67		Jang et al. (2015)
Zn-HCF	24.5		Sommer-Marquez et al. (2016)
Zn-Co PBA	255		Liu et al. (2017)
PB/NHBC	125.31		Li et al. (2020)
MnO$_2$		40.5	Valsala et al. (2010)
MnO$_2$-Sb$_2$O$_5$		30.2	Zhang et al. (2016)
PBA/Chitosan/CNTs	219.8	205.1	Li et al. (2016)
PB nanorod	194.26	256.62	This study

As shown in Table 4, the calculated $\Delta G°$ value were − 21.72, − 21.35, and − 20.26 kJ mol^{-1} in Cs^+ and − 20.87, − 20.37, and − 20.35 kJ mol^{-1} in Sr^{2+} at 298, 303 and 308 K, respectively. The negative $\Delta G°$ value confirmed that the adsorption process occurred spontaneously. The value of $\Delta G°$ increased with the temperature rise, indicating that high temperature in favor of adsorption. These results were similar to the experiment data (Wibowo et al. 2017). $\Delta H°$ and $\Delta S°$ give an insight into type and mechanism of adsorption process. The negative $\Delta H°$ value suggested the exothermic nature of adsorption. In general, the adsorption process was physical adsorption if $2.1 < \Delta H° < 20.9$ kJ mol^{-1}. If $\Delta H° > 80$ kJ mol^{-1}, the adsorption process was chemical adsorption (Hu et al. 2021). The obtained value of $\Delta H°$ was − 59.05 and − 51.12 kJ mol^{-1} and all between 20.9 and 80 kJ mol^{-1}; it perhaps attributed to the adsorption mechanism of Cs^+ and Sr^{2+} for PB nanorod being close to chemical adsorption; ions were caged in lattice defect of PB nanorod. In addition, the negative $\Delta S°$ value reflected the decreased randomness at the solid-solution interface during adsorption process.

Effect of pH

In general, iron hexacyanoferrate (Fe–Fe PB) was rapidly converted into Fe(OH)$_3$ in alkaline solution; it was ascribed to ion exchange reaction between Fe(III) and OH$^-$, as shown in the following equation (Zhang et al. 2013).

$$Fe_4[Fe(CN)_6]_{3(s)} + 12OH^-_{(aq)} \rightarrow 3Fe(CN)_6^{4-}{}_{(aq)} + 4Fe(OH)_{3(s)}$$
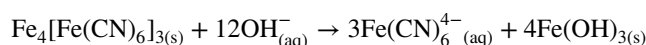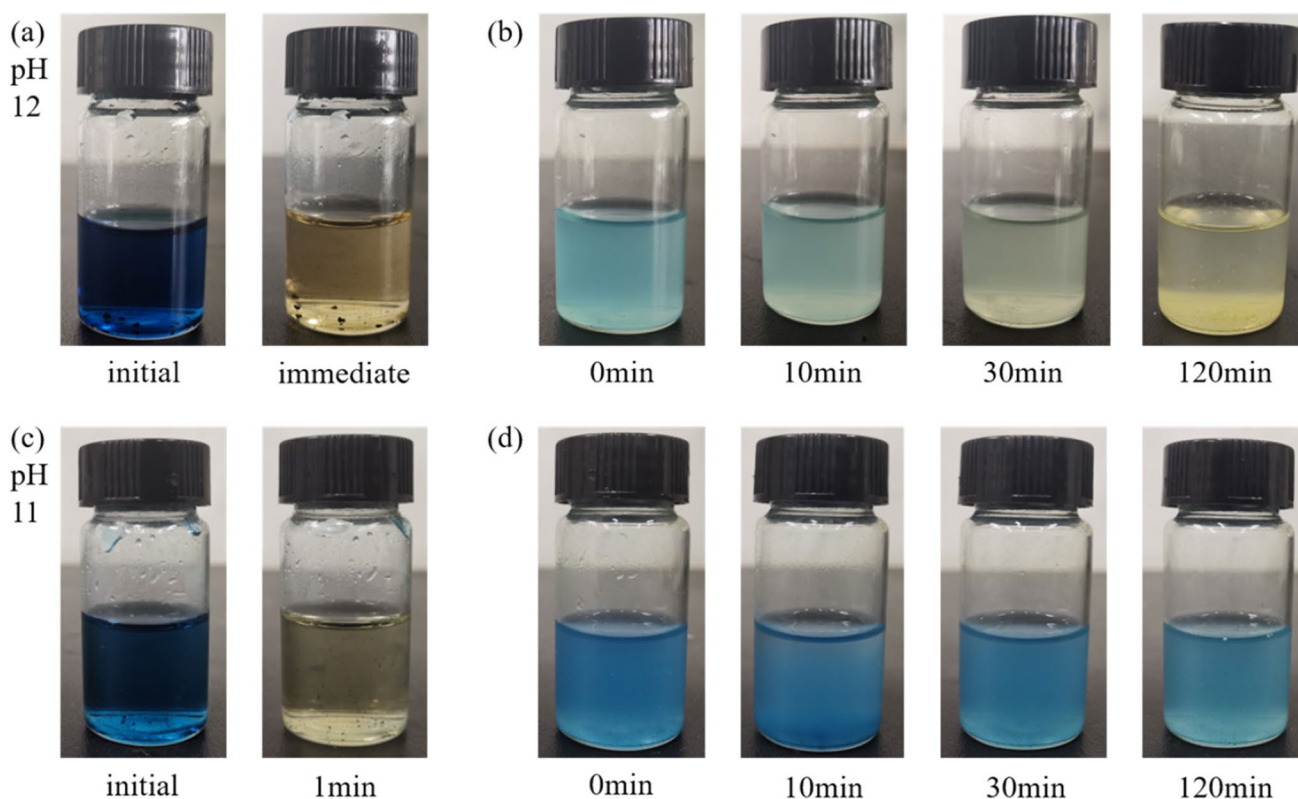
However, we obtained Fe–Fe PB nanorod that possessed a part of resistance to alkaline solution. In Fig. 7a and c, the color of solution which contained Fe–Fe PB changed from blue to yellow immediately when the solution is pH 12 and 11; it was meant that Fe–Fe PB obtained by co-precipitation was immediately transformed to Fe(OH)$_3$. In contrast, PB nanorod was stable, and solution color was not changed at initial pH = 12; after 10 min, the color started to turn yellow, and all of the PB nanorods transformed FeOH$_3$ until 120 min. When pH value was down to 11, the solution color remained blue throughout the whole process, showing the excellent stability of PB nanorod in alkaline solution. In general, the chemical etching process was prone to occur on the loose region of crystal, which possessed more defects (Nai et al. 2017; Shi et al. 2021; H. Xu et al. 2020; Yu et al. 2016). As shown in TEM image and XRD pattern, the high crystallization and low defect of PB nanorod slow down the erosion from hydroxyl ions.

In order to investigate the adsorption performance of PB nanorod at various pH values, the experiments were conducted at different pH values from 1 to 10 since Sr^{2+} was precipitated when pH was above 10 (Li et al. 2021). The result was shown in Fig. 8; the adsorption capacity of PB increased with pH value increasing from 1 to 5 both Cs^+ and Sr^{2+}, and then the adsorption amount of Sr^{2+} reached a maximum at pH of 7 and Cs^+ at pH of 8; after that the adsorption capacity decreased with pH value increased.

Table 4 Thermodynamic parameters of PB nanorod

| Absorbed element	T (K)	Thermodynamic parameters		
		ΔG (kJ mol^{-1})	ΔH (kJ mol^{-1})	ΔS (J mol^{-1} K^{-1})
	298	− 21.72		
Cs^+ sorption	303	− 21.35	− 59.05	− 125.01
	308	− 20.26		
	298	− 20.87		
Sr^{2+} sorption	303	− 20.37	− 51.12	− 101.49
	308	− 20.35		

Fig. 7 Time-dependent photographs of PB and PB nanorod in alkaline solution

The solution pH affected the degree of ionization and surface charge of the adsorbent, which could affect adsorption capacity. In acidic pH, the surface charge of adsorbent changed positively. It hindered the cation that entered the inner crystal, causing the adsorption amount to decrease. In an alkaline solution, the adsorbent surface changed negative, but the Prussian blue framework was unstable, leading to a decrease in adsorption capacity.

Effect of co-existing ions

Radioactive wastewater generally contains a large amount of co-existing ions like Na^+, K^+, Mg^{2+}, and Ca^{2+}. We investigated the effect of those ions on adsorption performance. As shown in Fig. 9, the different cations had different adsorption effect on Cs^+ and Sr^{2+}. K^+ played an important role in the process of Cs^+ being absorbed; the higher the concentration of K^+, the lower the K_d value of PB. Na^+ had little effect on adsorption amount owing to the stokes radii of Na^+ being smaller than K^+. While the Sr^{2+} was adsorbed, alkaline-earth metal ions had stronger resistance to adsorption than alkali metal ions. The K_d value were less than 1L g^{-1} both Mg^{2+} and Ca^{2+}. Otherwise, the electrostatic attraction could affect the ions adsorption process. The order of charged density was $Ca^{2+} > Mg^{2+} > K^+ > Na^+$ (Zhang et al. 2016), following the result of Sr^{2+} adsorption experiment.
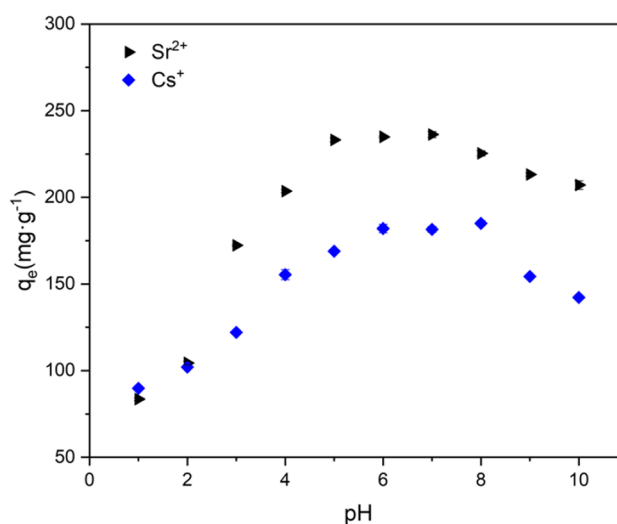
Fig. 8 Effect of initial pH on Cs^+ and Sr^{2+} adsorption capacity by PB nanorod

The distribution coefficient K_d was often used to present the chemical binding affinity between ions and adsorbents. Ordinarily, the K_d value above 5000 mL g^{-1} was considered good, and more than 50,000 mL g^{-1} was considered

excellent (Jang and Lee 2016). In this study, the obtained K_d value in different ions was all greater than 5000 mL g^{-1} in low and medium co-existing ion concentrations that showed a strong affinity between Cs$^+$, Sr^{2+}, and PB nanorod. Furthermore, the K_d value of PB nanorod for Cs$^+$ and Sr^{2+} sorption was 6.52 and 7.49 L g^{-1} in artificial seawater when $C_0 = 50$ ppm, V/M = 1L g^{-1}, and pH of 7; the result suggested that a high concentration of co-existing ions has little impact on the binding of Cs$^+$ and Sr^{2+} on PB nanorod.

Mechanism of adsorption

In the past decade, many researchers studied the adsorption mechanism of PB for Cs$^+$; some of them assumed that Cs$^+$ exchanged with K$^+$ in PB inner crystal structure, and others suggested that Cs$^+$ was trapped in PB crystal lattice (Ishizaki et al. 2013; Li et al. 2020). Moreover, the research about Prussian blue adsorbed Sr^{2+} was rarely mentioned. In order to reveal the Cs$^+$ and Sr^{2+} sorption mechanism to PB nanorods, 10 mg adsorbent was immersed in 10 mL 500 mg L^{-1} Cs$^+$ or Sr^{2+} aqueous solution for 6 h at 298 K, and the solution's initial pH was 7.0. Finally, the adsorbent was separated, the ion concentrations of Cs$^+$, Sr^{2+}, K$^+$, Fe^{2+}/Fe^{3+}, and the solution pH were measured, and the change values were listed in Table 5. The result showed that, before and after Cs$^+$ sorption, the Fe elements concentration did not change, and the increased value of K$^+$ concentration was similar to ΔCs$^+$. The pH value of the solution increased slightly after Cs$^+$ adsorption. On the contrary, the K concentration and pH value did not change, the Fe concentration increased dramatically, probably due to the iron escape from Prussian blue. Further research was then carried out with XPS and Mössbauer spectrum.

The detailed surface chemistry change of PB nanorods after adsorption was revealed by XPS analysis. Figure 10a shows the XPS spectrum of Prussian blue nanorod after Cs$^+$ and Sr^{2+} adsorption. Figure 10b is high-resolution N1S spectra. All spectra of three samples showed two peaks at 397.8 and 402.4 eV which were assigned to C≡N–Fe ligand and pyrrolic-N, respectively (Qian et al. 2017). Interestingly, the C≡N–Fe ligand peak shifted to 403 eV after Cs$^+$ adsorption, which could attribute to Cs$^+$ being bonded with the cyano group. All Fe2p spectra of pristine, after Cs$^+$ and Sr^{2+} adsorption PB nanorods, gave four peaks which presented two valences of Fe element (Wang et al. 2019). The peaks located at 708.96 and 721.70 eV could be indexed to Fe^{II} in Fe 2P$_{3/2}$ and Fe 2P$_{1/2}$. At about 710.48 and 723.82 eV, the other two were assigned to Fe^{III} in Fe 2P$_{3/2}$ and Fe 2P$_{1/2}$. The element's peak area of the XPS spectrum expressed a relative quantity of different valences. The table summarizes the peak area of each sample. We could see that the pristine PB nanorod total peak area of Fe^{III} only accounts for 0.32 of that Fe^{II}. By contrast, the content ratio
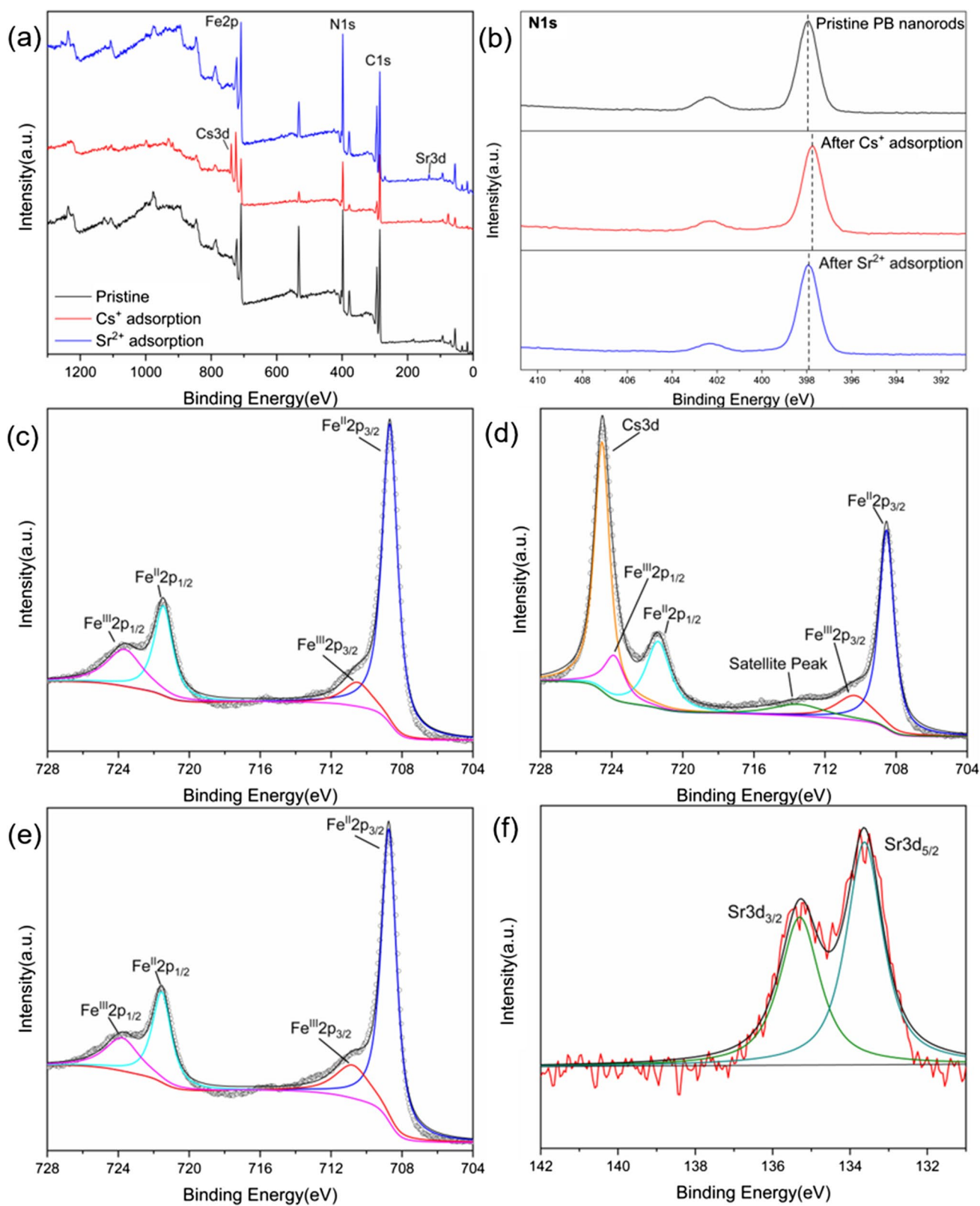
Table 5 The change values of ions concentration before and after adsorption

Adsorbate	ΔAdsorbate (mmol/L)	ΔK$^+$ (mmol/L)	ΔFe (mmol/L)	pH
Cs$^+$	−1.53	+1.41	+0.03	7.1
Sr^{2+}	−3.01	+0.02	+0.76	7.0
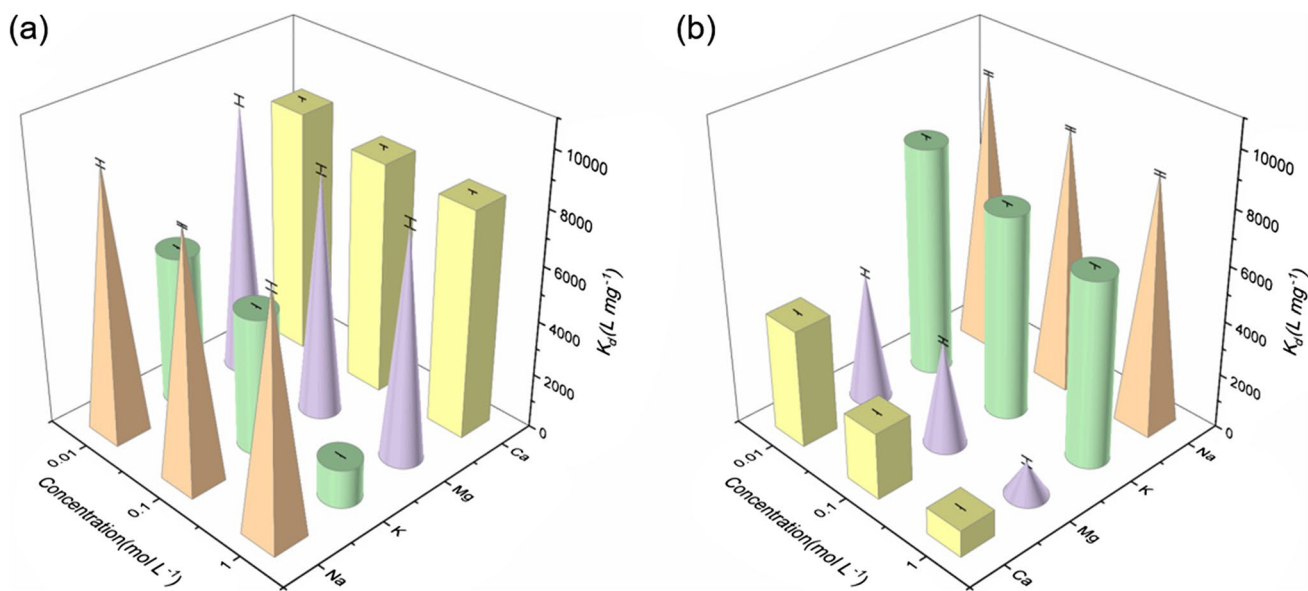
Fig. 9 The effect of co-existing Na$^+$, K$^+$, Mg^{2+}, and Ca^{2+} on the removal efficiency of PB nanorod for Cs$^+$ (**a**) and Sr^{2+} (**b**)

Fig. 10 XPS survey spectra of PB nanorod (**a**), N 1 s spectra (**b**), Fe 2p spectra of PB nanorods (**c**), after Cs^+ adsorption (**d**) and after Sr^{2+} adsorption (**e**), Sr 3d spectra (**f**)

Table 6 XPS fitting results of Fe element

Samples	Peak area				Fe^{III}/Fe^{II}
	$Fe^{II}2p_{3/2}$	$Fe^{II}2p_{1/2}$	$Fe^{III}2p_{3/2}$	$Fe^{III}2p_{1/2}$	
PB nanorod	602.3	220.6	90.4	172.9	0.32
Cs^+ adsorption	267.6	147.5	79.8	83.7	0.39
Sr^{2+} adsorption	696.9	271.3	181.8	175.0	0.37

Table 7 Mössbauer spectrum fitting results

Sample	Valence	IS (mm s^{-1})	QS (mm s^{-1})	ARE (%)
Pristine	Fe^{2+}	−0.15822		41.95
	Fe^{3+}	0.38089	0.48227	58.05
Cs^+ sorption	Fe^{2+}	−0.14608		46.53
	Fe^{3+}	0.38956	0.42485	53.46
Sr^{2+} sorption	Fe^{2+}	−0.15019		39.87
	Fe^{3+}	0.36832	0.42149	60.13

of Fe^{III} to Fe^{II} on the surface of PB nanorod after Cs^+ and Sr^{2+} adsorption improved to 0.39 and 0.37. This result indicated that Prussian blue released some Fe^{2+} in adsorption process. As shown in the Cs3d spectra of PB nanorod after Cs^+ adsorption, two peaks at 725 and 730 eV were allocated to Cs $3d_{3/2}$ and Cs $3d_{5/2}$. Figure 10f displays high-resolution Sr3d spectra, with two peaks at 133.93 eV and 135.64 eV characteristic for $3d_{3/2}$ and $3d_{1/2}$ of strontium.

XPS only detected the surface elements instead of penetrating deep into the sample, and the Mössbauer spectrum gave an over-arching perspective of the iron valence inside the whole sample (Hu et al. 2012a, b). In Mössbauer spectrum analysis, the pristine PB contained 41.95% Fe(II) and 58.05% Fe(III); there were 46.53% Fe(II) and 53.46% Fe(III) in PB nanorod; after Sr^{2+} adsorption, there were 39.87% Fe(II) and 60.13% Fe(III). The Fe^{2+} content of PB only decreased by 2.08% after Sr^{2+} adsorption, which was lower than XPS result; the XRD pattern of PB also did not change; it was demonstrated that Sr^{2+} was mainly caged in the PB framework and surface ions exchange was a small proportion. After Cs^+ adsorption, there were 46.53% Fe(II) and

53.46% Fe(III) in PB nanorod; the change of Fe content was larger than Sr^{2+} adsorption before and after. Interestingly, the XRD pattern of PB after Cs^+ adsorption was different from the other two; this indexed to $CsFe[Fe(CN)_6]$(JCPDS 24–0259) rather than $Fe_3[Fe(CN)_6]_4$(JCPDS 73–0687), and a similar result was also obtained by the stoichiometry change of Fe^{2+} and Fe^{3+} for PB nanorod before and after adsorption Cs^+ (Table 6, Fig. 11).

Based on the above result (Table 7), Scheme 1 illustrated the different adsorption mechanisms of two cations. Firstly, Cs^+ could enter the crystal inner, causing the PB structure to be transferred from insoluble to soluble because that structure possessed a greater capacity for monovalent ions. Secondly, Sr^{2+} also entered the PB crystal to achieve decontamination, which did not lead to structural change. In addition, corresponding to the surface element change from XPS, we could infer that part of Sr^{2+} exchanged with Fe^{2+} on the PB surface. According to the adsorption mechanism, the theoretical adsorption capacity of PB for Cs^+ was

Fig. 11 Mössbauer spectrum of PB nanorod before and after Cs^+ and Sr^{2+} adsorption
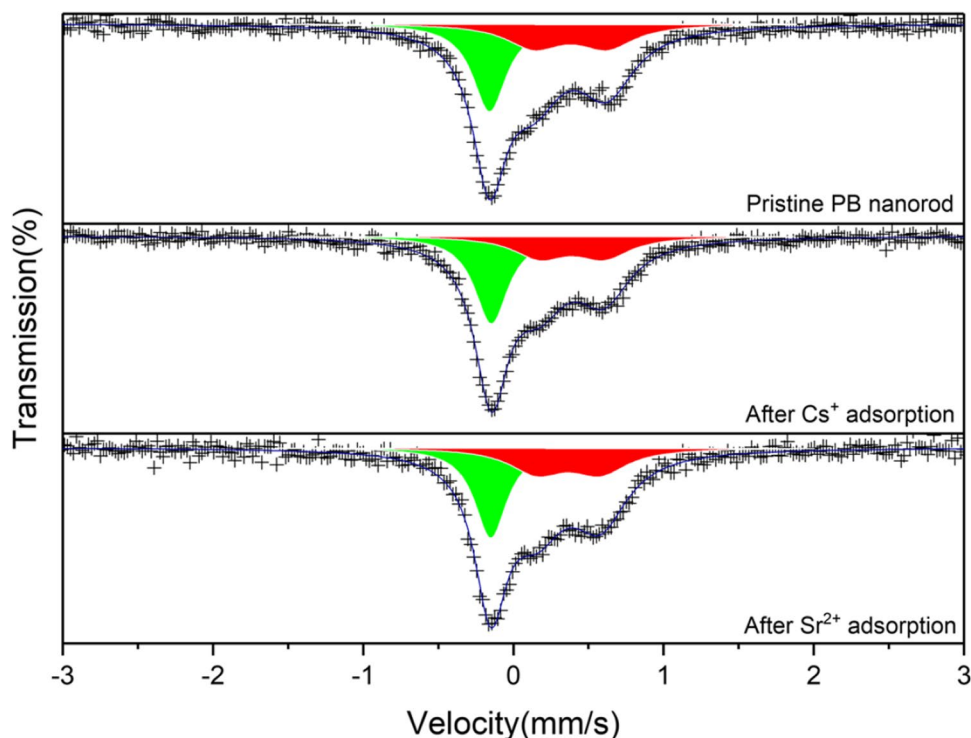
Scheme 1 Illustration of adsorption mechanism
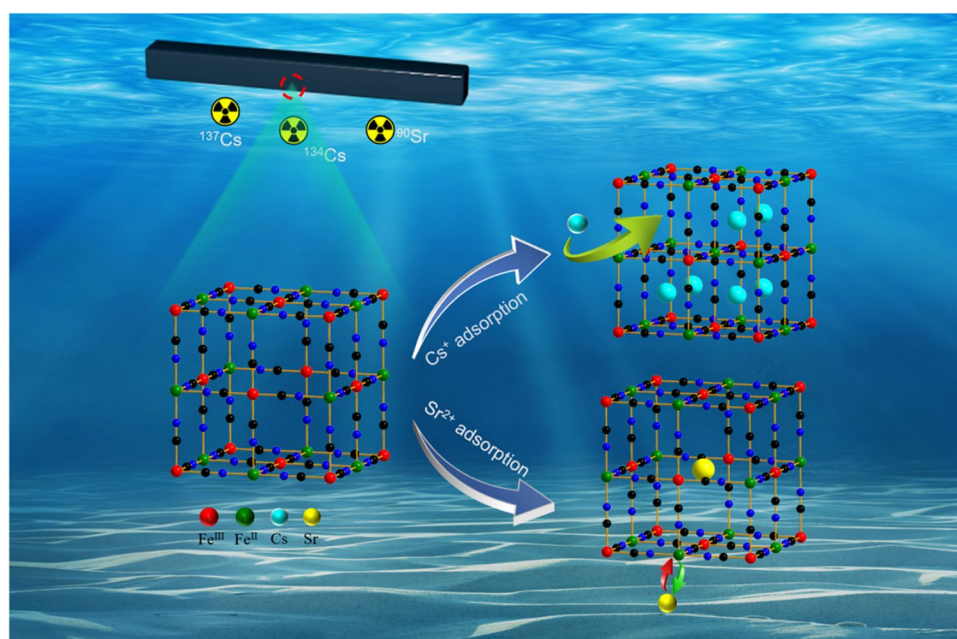
larger than Sr^{2+}. Contrary to the experimental result, it could ascribe to the electrostatic interaction between Sr^{2+} and surface residual $-COOH$ derived from glucose being reduced.

Conclusion

In this work, PB nanorods were synthesized by hydrothermal microemulsion and applied to adsorb cesium and strontium in simulated radioactive wastewater. Prussian blue nanorod showed a better removal efficiency of Cs^+ and Sr^{2+} than ordinary Prussian blue, the adsorption data were described well with Langmuir isotherm and pseudo-second-order equation; the maximum adsorption capacity of PB nanorod was estimated to be 194.26 mg g^{-1} and 256.62 mg g^{-1} for Cs^+ and Sr^{2+} (adsorbate concentration at 500 mg L^{-1}, the temperature at 298 k, pH at 7.0). The thermodynamic analysis indicated that the adsorption process was spontaneous and endothermic in nature. Moreover, HRTEM and SAED results showed that PB nanorods had high crystallinity and few crystal defects, giving them good stability under alkaline conditions. The analysis result by XPS, XRD, and ^{57}Fe Mössbauer spectrum revealed that Cs^+ entered in PB crystal to generate a new phase; most of Sr^{2+} was trapped in the internal crystal, and the other exchanged Fe^{2+}. Therefore, PB nanorod was an outstanding candidate for removing Cs^+ and Sr^{2+} from radioactive wastewater.

Author contribution Chuqing Yao: data curation, writing-original draft. Yaodong Dai: conceptualization, supervision, writing—review and editing. Shuquan Chang: writing—review and editing. Haiqian Zhang: writing—review and editing.

Declarations

Ethics approval and consent to participate Not applicable.

Consent for publication Not applicable.

Competing interests The authors declare no competing interests.

References

Ahrouch M, Gatica JM, Draoui K, Bellido D, Vidal H (2019) Lead removal from aqueous solution by means of integral natural clays honeycomb monoliths. J Hazard Mater 365:519–530

Andrew Lin K-Y, Yang H, Lee W-D (2015) Enhanced removal of diclofenac from water using a zeolitic imidazole framework functionalized with cetyltrimethylammonium bromide (CTAB). RSC Adv 5(99):81330–81340

Bu F-X, Hu M, Zhang W, Meng Q, Xu L, Jiang D-M et al (2015) Three-dimensional hierarchical Prussian blue composed of ultrathin nanosheets: enhanced hetero-catalytic and adsorption properties. Chem Commun 51(99):17568–17571

Cai D, Liu B, Wang D, Wang L, Liu Y, Qu B et al (2016) Rational synthesis of metal–organic framework composites, hollow structures and their derived porous mixed metal oxide hollow structures. J Mater Chem A 4(1):183–192

Cheng R, Kang M, Zhuang S, Shi L, Zheng X, Wang J (2019) Adsorption of Sr(II) from water by mercerized bacterial cellulose membrane modified with EDTA. J Hazard Mater 364:645–653

Demirbas E, Dizge N, Sulak MT, Kobya M (2009) Adsorption kinetics and equilibrium of copper from aqueous solutions using hazelnut shell activated carbon. Chem Eng J 148(2–3):480–487

Falyouna O, Eljamal O, Maamoun I, Tahara A, Sugihara Y (2020) Magnetic zeolite synthesis for efficient removal of cesium in a lab-scale continuous treatment system. J Colloid Interface Sci 571:66–79

Feng Y, Wang X, Dong P, Li J, Feng L, Huang J et al (2019) Boosting the activity of Prussian-blue analogue as efficient electrocatalyst for water and urea oxidation. Sci Rep 9(1):15965

Gupta K, Yuan B, Chen C, Varnakavi N, Fu M-L (2019) $K_{2x}Mn_xSn_{3-x}S_6$ (x = 0.5–0.95) (KMS-1) immobilized on the reduced graphene oxide as KMS-1/r-GO aerogel to effectively remove Cs^+ and Sr^{2+} from aqueous solution. Chem Eng J 369:803–812

Hu L, Mei JY, Chen QW, Zhang P, Yan N (2011) Magnetically separable Prussian blue analogue Mn3[Co(CN)$_6$]$_2$.nH2O porous nanocubes as excellent absorbents for heavy metal ions. Nanoscale 3(10):4270–4274

Hu M, Belik AA, Imura M, Mibu K, Tsujimoto Y, Yamauchi Y (2012a) Synthesis of superparamagnetic nanoporous iron oxide particles with hollow interiors by using Prussian blue coordination polymers. Chem Mater 24(14):2698–2707

Hu M, Belik AA, Imura M, Yamauchi Y (2013) Tailored design of multiple nanoarchitectures in metal-cyanide hybrid coordination polymers. J Am Chem Soc 135(1):384–391

Hu M, Furukawa S, Ohtani R, Sukegawa H, Nemoto Y, Reboul J et al (2012b) Synthesis of Prussian blue nanoparticles with a hollow interior by controlled chemical etching. Angew Chem Int Ed Engl 51(4):984–988

Hu YY, Pan C, Zheng X, Hu F, Xu L, Xu G et al (2021) Prediction and optimization of adsorption properties for Cs^+ on NiSiO@NiAlFe LDHs hollow spheres from aqueous solution: kinetics, isotherms, and BBD model. J Hazard Mater 401:123374

Ishizaki M, Akiba S, Ohtani A, Hoshi Y, Ono K, Matsuba M et al (2013) Proton-exchange mechanism of specific Cs^+ adsorption via lattice defect sites of Prussian blue filled with coordination and crystallization water molecules. Dalton Trans 42(45):16049–16055

Jang J, Lee DS (2016) Magnetic Prussian blue nanocomposites for effective cesium removal from aqueous solution. Ind Eng Chem Res 55(13):3852–3860

Jang S-C, Haldorai Y, Lee G-W, Hwang S-K, Han Y-K, Roh C et al (2015) Porous three-dimensional graphene foam/Prussian blue composite for efficient removal of radioactive ^{137}Cs. Sci Rep 5(1):17510

Ji C, Ren Y, Yu H, Hua M, Lv L, Zhang W (2022) Highly efficient and selective Hg(II) removal from water by thiol-functionalized MOF-808: kinetic and mechanism study. Chem Eng J 430:132960

Jin Y, Liu F, Tong M, Hou Y (2012) Removal of arsenate by cetyltrimethylammonium bromide modified magnetic nanoparticles. J Hazard Mater 227–228:461–468

Kim DS, Zakaria MB, Park M-S, Alowasheeir A, Alshehri SM, Yamauchi Y et al (2017) Dual-textured Prussian blue nanocubes as sodium ion storage materials. Electrochim Acta 240:300–306

Li J, Zan Y, Zhang Z, Dou M, Wang F (2020) Prussian blue nanocubes decorated on nitrogen-doped hierarchically porous carbon network for efficient sorption of radioactive cesium. J Hazard Mater 385:121568

Li T, He F, Dai Y (2016) Prussian blue analog caged in chitosan surface-decorated carbon nanotubes for removal cesium and strontium. J Radioanal Nucl Chem 310(3):1139–1145

Li WA, Li JR, Zhang B, Sun HY, Jin JC, Huang XY et al (2021) Layered thiostannates with distinct arrangements of mixed cations for the selective capture of Cs^+, Sr^{2+}, and Eu^{3+} ions. ACS Appl Mater Interfaces 13(8):10191–10201

Liu J, Li X, Rykov AI, Fan Q, Xu W, Cong W et al (2017) Zinc-modulated Fe–Co Prussian blue analogues with well-controlled morphologies for the efficient sorption of cesium. J Mater Chem A 5(7):3284–3292

Liu Y (2009) Is the free energy change of adsorption correctly calculated? J Chem Eng Data 54(7):1981–1985

Liu Y, Qiao Y, Zhang W, Li Z, Ji X, Miao L et al (2015) Sodium storage in Na-rich Na$_x$FeFe(CN)$_6$ nanocubes. Nano Energy 12:386–393

Minitha CR, Suresh R, Maity UK, Haldorai Y, Subramaniam V, Manoravi P et al (2018) Magnetite nanoparticle decorated reduced graphene oxide composite as an efficient and recoverable adsorbent for the removal of cesium and strontium ions. Ind Eng Chem Res 57(4):1225–1232

Nai J, Lu Y, Yu L, Wang X, Lou XWD (2017) Formation of Ni-Fe mixed diselenide nanocages as a superior oxygen evolution electrocatalyst.Adv Mater 29(41):1703870

Qian J, Cai S, Yang S, Hua D (2017) A thermo-sensitive polymer network crosslinked by Prussian blue nanocrystals for cesium adsorption from aqueous solution with large capacity. J Mater Chem A 5(42):22380–22388

Shi C, Ye S, Wang X, Meng F, Liu J, Yang T et al (2021) Modular construction of Prussian blue analog and TiO$_2$ dual-compartment Janus nanoreactor for efficient photocatalytic water splitting. Adv Sci (weinh) 8(7):2001987

Sommer-Marquez A, Mansas C, Talha N, Rey C, Causse J (2016) Reinforced silica monoliths functionalised with metal hexacyanoferrates for cesium decontamination: a combination of a one-pot procedure and skeleton calcination. RSC Adv 6(77):73475–73484

Tiwari JN, Tiwari RN, Kim KS (2012) Zero-dimensional, one-dimensional, two-dimensional and three-dimensional nanostructured materials for advanced electrochemical energy devices. Prog Mater Sci 57(4):724–803

Valsala TP, Joseph A, Sonar NL, Sonavane MS, Shah JG, Raj K et al (2010) Separation of strontium from low level radioactive waste solutions using hydrous manganese dioxide composite materials. J Nucl Mater 404(2):138–143

Vaucher S, Li M, Mann S (2000) Synthesis of Prussian blue nanoparticles and nanocrystal superlattices in reverse microemulsions. Angew Chem Int Ed Engl 39(10):1793–1796

Wang N, Ma W, Du Y, Ren Z, Han B, Zhang L et al (2019) Prussian blue microcrystals with morphology evolution as a high-performance photo-Fenton catalyst for degradation of organic pollutants. ACS Appl Mater Interfaces 11(1):1174–1184

Wibowo E, Rokhmat M, Sutisna K, Abdullah M (2017) Reduction of seawater salinity by natural zeolite (Clinoptilolite): adsorption isotherms, thermodynamics and kinetics. Desalination 409:146–156

Wu X, Cao M, Hu C, He X (2005) Sonochemical synthesis of Prussian blue nanocubes from a single-source precursor. Cryst Growth Des 6(1):26–28

Xiong Y, Cai H, Wiley BJ, Wang J, Kim MJ, Xia Y (2007) Synthesis and mechanistic study of palladium nanobars and nanorods. J Am Chem Soc 129(12):3665–3675

Xiong Y, Xia Y (2007) Shape-controlled synthesis of metal nanostructures: the case of palladium. Adv Mater 19(20):3385–3391

Xu D, Liu Z, Liang J, Qian Y (2005) Solvothermal synthesis of CdS nanowires in a mixed solvent of ethylenediamine and dodecanethiol. J Phys Chem B 109(30):14344–14349

Xu H, Zhao X, Yu C, Sun Y, Hui Z, Zhou R et al (2020) Mechanistic insight in site-selective and anisotropic etching of Prussian blue analogues toward designable complex architectures for efficient energy storage. Nanoscale 12(20):11112–11118

Yang H, Sun L, Zhai J, Li H, Zhao Y, Yu H (2014) In situ controllable synthesis of magnetic Prussian blue/graphene oxide nanocomposites for removal of radioactive cesium in water. J Mater Chem A 2(2):326–332

Yin X, Li H, Wang H, Zhang Z, Yuan R, Lu J et al (2018) Self-templating synthesis of cobalt hexacyanoferrate hollow structures with superior performance for Na-Ion hybrid supercapacitors. ACS Appl Mater Interfaces 10(35):29496–29504

Yu XY, Feng Y, Jeon Y, Guan B, Lou XW, Paik U (2016) Formation of Ni-Co-MoS$_2$ nanoboxes with enhanced electrocatalytic activity for hydrogen evolution. Adv Mater 28(40):9006–9011

Zhang F, Song W, Lan J (2015) Effective removal of methyl blue by fine-structured strontium and barium phosphate nanorods. Appl Surf Sci 326:195–203

Zhang L, Wei J, Zhao X, Li F, Jiang F, Zhang M et al (2016) Removal of strontium(II) and cobalt(II) from acidic solution by manganese antimonate. Chem Eng J 302:733–743

Zhang L, Wu HB, Xu R, Lou XW (2013) Porous Fe2O3 nanocubes derived from MOFs for highly reversible lithium storage. CrystEngComm 15(45):9332–9335

Zhou P, Xue D, Luo H, Chen X (2002) Fabrication, structure, and magnetic properties of highly ordered prussian blue nanowire arrays. Nano Lett 2(8):845–847